Electrochemical impedance spectroscopy analysis of a thin polymer film-based micro-direct methanol fuel cell

Tobias Schulz, Christian Weinmüller, Majid Nabavi, Dimos Poulikakos *

Department of Mechanical and Process Engineering, Laboratory of Thermodynamics in Emerging Technologies, Institute of Energy Technology, ETH Zurich, CH-8092 Zurich, Switzerland

ARTICLE INFO

ABSTRACT

A single cell micro-direct methanol fuel cell (micro-DMFC) was investigated using electrochemical impedance spectroscopy. The electrodes consisted of thin, flexible polymer (SU8) film microchannel structures fabricated in-house using microfabrication techniques. AC impedance spectroscopy was used to separate contributions to the overall cell polarization from the anode, cathode and membrane. A clear distinction between the different electrochemical phenomena occurring in the micro-DMFC, especially the distinction between double layer charging and Faradaic reactions was shown. The effect of fuel flow rate, temperature, and anode flow channel structure on the impedance of the electrode reactions and membrane/electrode double layer charging were investigated. Analysis of impedance data revealed that the performance of the test cell was largely limited by the presence of intermediate carbon monoxide in the anode reaction. Higher temperatures increase cell performance by enabling intermediate CO to be oxidized at much higher rates. The results also revealed that serpentine anode flow microchannels show a lower tendency to intermediate CO coverage and a more stable cell behavior than parallel microchannels.

1. Introduction

The past decade has shown a high level of interest in research on direct methanol fuel cells (DMFC). It is believed that they can deliver a high energy density power supply [1,2]. Miniaturization possibilities and improvement in microfabrication techniques have also helped to drive research in micro-DMFC [3–6]. The present work is focussed on diagnostics of a micro-DMFC with microfabricated polymer electrodes. In the past, DMFC diagnostics have been limited to DC electrochemical techniques such as potential step, current interruption and steady state polarization curve techniques [7]. The information gained from these techniques is practically confined to an aggregate of performance hindering mechanisms in the cell including mass transport, charge separation, charge transfer, electronic and ionic resistances and does not allow experimental insight into a break down of this information [7]. Electrochemical impedance spectroscopy (EIS) is used in many fields of electrochemical research. In fuel cell research, EIS has mainly been concentrated on hydrogen polymer electrolyte membrane fuel cells (PEMFC) with countless publications on nearly every aspect of a PEMFC available [8–15]. A very convenient assumption, i.e. that the hydrogen reaction on the anode side can be neglected compared to the oxygen reaction on the cathode, simplified impedance analysis of PEMFC greatly and thus led to enhanced interest in the diagnostic technique. It was even taken as far as being developed as an on-board automated diagnostic system for commercial PEMFC stacks [16].

Much less activity has been reported on EIS for DMFCs. A thorough literature search yields only a few publications. They can mainly be divided into two categories: those on general DMFC systems [17–21] and others focussing on specifics such as structural or operational factors [22–28]. On the whole, EIS has had a modest influence on DMFC diagnostics compared to that of direct hydrogen fuel cell (DHFC). The reasons behind this are quite likely to be the need to be able to measure the impedance of anode and cathode separately and the much more complex chemical reaction taking place at the anode. Separating anode and cathode contributions has always been associated with introducing a reference electrode into the cell configuration. Indeed this is the subject of the work by Diard et al. [19] in which they used a reference electrode in a DMFC to separate anode and cathode impedances. However, the packaging and correct placement of such a reference electrode is not always easy and causes significant problems when cells are scaled down in size. Consequently practical implementation of a reference electrode is extremely difficult in micro-fuel cells and has not been reported in literature either. Moreover, operational stability of the

* Corresponding author. Tel.: +41 44 632 2738; fax: +41 44 632 1176.
E-mail address: dimos.poulikakos@ethz.ch (D. Poulikakos).

fuel cell is an absolute prerequisite for a successful impedance analysis and is increasingly difficult to achieve as cells are miniaturized. Müller and Urban provided a breakthrough in terms of impedance spectroscopy on DMFCs [17]. They took the assumption used in DHFC EIS that the hydrogen reaction can be neglected when compared to the oxygen reaction and applied it to DMFC by creating a dynamic hydrogen reference electrode. EIS for micro-DMFC has been reported in only one study [29], in which the authors only measured the anode spectrum of a passive micro-DMFC with a new anodic diffusive layer in order to identify the effects of anodic microporous layer materials on the cell performance.

As the literature review indicates, the use of EIS on methanol fuel cells is fairly limited and confined to a handful of studies. However, only one study has provided a brief analysis of EIS on micro-DMFC [29]. As in the other studies using EIS, equivalent circuits are employed in the present study to analyze the experimental data. The equivalent circuits in this study are partly derived from previous publications on DMFC EIS, but also include novel circuit elements such as the Warburg element in both the anode charge transfer reaction and the double layer capacitance circuit. On the cathode side, an equivalent circuit for the charge transfer reaction is proposed, which has not yet been seen in the literature. The exclusion of inductive elements in this circuit is argued by making an attempt to verify the method introduced in [17] by recording spectra in the classical DHFC configuration. Of particular interest with regards to previous disagreements in literature on EIS DMFC studies are the membrane and electrode interface results, anode charge transfer capacitance values and the presence of methanol crossover in the calculated cathode spectra.

2. Material and methods

2.1. Experimental setup

Fig. 1 provides a schematic overview of the experimental setup. As can be seen the anode is fed with one molar solution of methanol (MeOH) via a syringe pump (1) and the cathode with pure oxygen (6) which is humidified in heated water in the bubbler (4). Both fuel and oxidant feeds were operated without back pressure control thus they were controlled by a constant volumetric feed rate from the syringe pump (1) and a constant mass flow rate from the oxygen mass flow controller (5).

On the electrical side there is a voltmeter (12), a load bank (11) and a frequency response analyzer used for the impedance measurements (10). Both the voltmeter and load bank are controlled

using LabVIEW software through the data acquisition interface (13). Similarly the oxygen gas mass flow valve (5) and heater elements are controlled via LabVIEW software on the PC. O_2 flow rate was 8 ml min^{-1} throughout the experiment. Three different values for MeOH flow rate and heater temperature were used (0.035, 0.14, and 0.56 ml min^{-1}, and 30, 60, and 90 °C). Four different values (8, 22, 36, and 60 mA cm^{-2}) were used for current density.

2.2. Fuel cell microfabrication

2.2.1. Anode

Two main designs were used for the microchannels on the anode side: serpentine and parallel. The width of the microchannels used in both the serpentine and parallel configurations was 300 μm. An epoxy-based negative photo resist (SU8) was used for the anode flow plate. SU8 is largely inert and able to withstand high temperatures. The following steps were performed in order to fabricate SU8 flow plates (also illustrated in Fig. 2): (1) a layer of LOR (sacrificial layer) was applied through the process of spin coating onto a silicon base wafer; (2) a 200-μm layer of SU8 was then spin coated onto the sacrificial layer; (3) the next step was exposure to UV light. A mask was used in this photolithographic step to cover the areas that should later be dissolved; (4) a thin layer of gold was then evaporated onto the SU8 surface using electron beam physical vapor deposition; (5) the sacrificial layer was dissolved thus releasing the SU8 layer from the silicon base wafer.

The sandwich structure design concept of the test cell allowed easy introduction of PDMS and PMMA layers to facilitate in and out flows of fluid and gas. The PDMS layer is soft allowing easy compression and contact with the anode flow plate. When using the parallel flow structure the PDMS layer behind the electrode was also needed as a part of the flow structure since a second plane was required to introduce and collect the fluid along the ribs. An SU8 parallel flow plate with PDMS and PMMA backing layers can be seen in Fig. 3.

The catalysts were directly applied onto the membrane surface over an area of 1 cm^2 (active area). The quoted loading for both the platinum-ruthenium combination on the anode side and platinum on the cathode is 4 mg cm^{-2}. Similar to the catalysts being directly applied on the membrane surface, the gas diffusion layer used on the cathode side in this work was also part of the membrane/catalyst assembly. It consisted of a thin carbon cloth structure hot pressed onto the cathode catalyst layer. The membrane material itself was Nafion 177, with the number corresponding to a thickness of 177 μm.
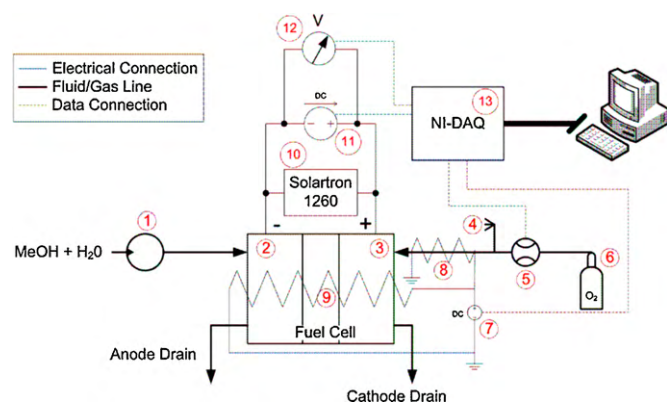

Fig. 1. Overview of experimental setup. (1) Harvard Apparatus PHD4400 Syringe Pump, (7) DC power source, (2) anode, (8) O_2 preheater, (3) cathode, (9) core heater, (4) humidifier, (10) Solartron FRA1260A, (5) Bronkhorst EL-flow mass flow controller, (11) Keithley 6221 current sink, (6) O_2 cylinder, (12) Keithley 2182A nanovoltmeter, (13) National Instruments data acquisition.
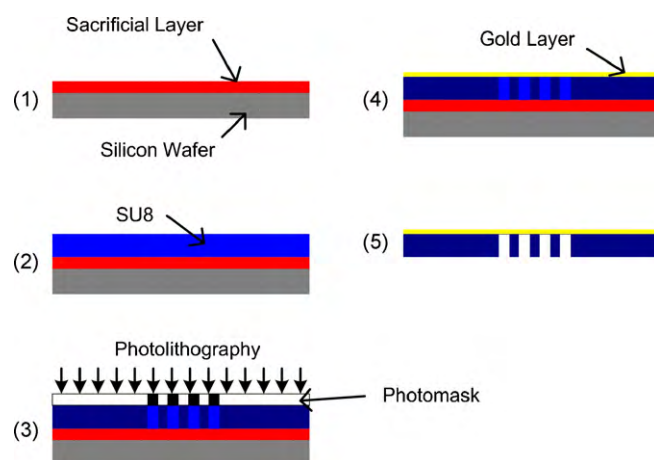

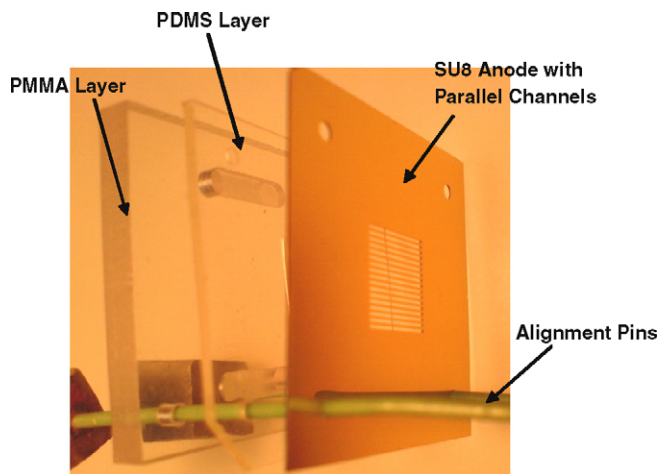**Fig. 2.** Graphical illustration of microfabrication steps.

Fig. 3. Picture of anode flow plate and anode backing.

2.2.2. Cathode

The structure and size of the cathode flow channels used in this work were not varied at all with a serpentine flow field of channel width 300 μm being the sole choice. The outcome of the previous work [30] showed that this flow pattern helped to increase stable performance of the cell substantially. As opposed to the SU8 structure of the anode, the cathode flow channels are etched into silicon in a MEMS process not explained here but can be found in [30]. The surface of the silicon flow plate was also covered in gold in the same way as the anode, giving it its electrically conductive property. To help increase ruggedness of the cathode flow plate, it was glued to a stainless steel backing plate which was then contacted electrically via a screw in the upper part of the holding frame (see Fig. 4).

2.2.3. Heater

Two heaters were used on the test cell: one to heat the core and the other to preheat the oxygen supply to the cathode. The latter was done to make sure that the moisture in the oxygen stream did not condense in the supply pipe. In the core the heating wire was fixed to an aluminium block with a thermally conductive glue. The heated aluminium block surrounded the core cell structure in the plane of the membrane electrode assembly, thus ensuring that the active area was heated uniformly.

2.3. Experimental procedure

The cell was assembled by putting together the relevant components discussed in Section 2.2. Since water content has a huge effect on the resistivity of the membrane (generally a better hydrated membrane decreases its resistance [31]), it was made sure that the membrane was sufficiently hydrated in deionized water before

being used in the cell. Once all electrical, gas and fluid connections were made to the cell, fuel and oxidant supplies were turned on and their rates adjusted to 8 ml min^{-1} for O_2 and one molar for MeOH. The cell was left at open circuit for approximately 10–20 min before any load was applied to make sure the temperature had reached its desired value and that the electrodes were sufficiently supplied with fuel and oxidant. Once the open circuit voltage had stabilized within ±1 mV a steady state polarization curve was recorded.

A program was created in LabVIEW to automatically record a steady state polarization curve. It used the galvanostatically controlled load bank (Keithley 6221) to set the operating point and monitored the voltage using a nanovoltmeter (Keithley 2182A). As soon as the cell had settled within the tolerance value for the specified duration (time window) the program would automatically increase the load by the specified current step. This would continue until the cell voltage falls to zero after which the cell was returned to open circuit. Once a steady state polarization curve had been recorded and the cell returned to open circuit conditions, the desired operating point for the impedance measurement was then found by using the same current step as in the polarization curve. Once the cell had stabilized at the desired operating point the impedance measurement was started.

Impedance curves could be recorded using a Solartron frequency response analyzer and the data displayed using ZPlot-Lab software. This software also allowed equivalent circuits to be fitted over the same frequency range giving the simulated results seen in Section 3.

2.4. Theory of anode and cathode impedance separation

As mentioned in the introduction, Müller and Urban [17] developed a method for separating anode and cathode contributions to impedance which has largely been followed by subsequent publications. It is also the method pursued in this study and this subsection aims to describe the theory behind it.

In hydrogen fuel cell research, the hydrogen oxidation reaction at the anode is said to happen with negligible impedance compared to the oxygen reduction reaction at the cathode [14]. Thus when measuring the impedance of a hydrogen fuel cell the measured data can be assumed to be the impedance of the oxygen reduction reaction. Following this theory, we can replace the oxygen gas stream in our DMFC with hydrogen and create a dynamic hydrogen reference electrode at the cathode. Methanol is still oxidized on the anode but now instead of oxygen being reduced at the cathode, hydrogen is generated. This mode of operation is termed *anode polarization* mode and is referred to as such hereafter. Since methanol oxidation takes place with a much higher impedance than the hydrogen evolution reaction, one can again assume the recorded impedance spectrum to be that of the methanol oxidation, i.e. the anode. In another test cycle the impedance of the full cell can be recorded, i.e. with the cell being supplied with its conventional fuel and oxidant
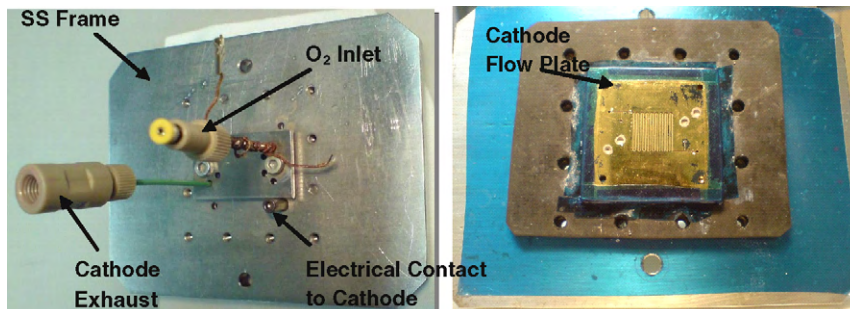

Fig. 4. Stainless steel frame on cathode side with fluid in/outlets (left), cathode serpentine flow plate (right).
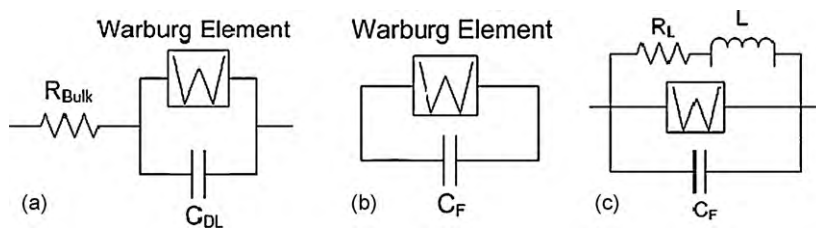
Fig. 5. The equivalent circuits for (a) double layer charging with diffusion behavior, (b) oxygen reduction with diffusion behavior, and (c) methanol oxidation with diffusion behavior.

streams. If the impedance spectrum of the anode is subtracted from that of the full cell then this should theoretically yield the cathode spectrum.

2.5. Development of equivalent circuits

EIS has become one of the most successful in-situ diagnostic methods for characterization of electrical properties and interfaces to electrodes. The impedance of a circuit is its opposition to the flow of alternating current. By analysing this property over a range of frequencies it is possible to untangle simultaneous processes happening at different rates. The general approach is to stimulate the object under observation with a known alternating current or voltage signal and consequently measure the response of the system. One of the reasons why EIS has achieved such significance in electrochemical research is that it facilitates comparisons between theoretically developed equivalent circuit models and models fitted to measured data thus allowing a detailed component by component analysis of the processes taking place in the system of interest. Numerous studies [16,32,33] have been devoted to the theoretical and empirical development of equivalent electrical circuits for all kinds of electrochemical sources. In this study, equivalent circuits using the finite length diffusion Warburg element were employed to help improve the fit between equivalent models and experimental data. By employing a finite length diffusion boundary condition the impedance of a Warburg element can be reduced to the following equation:

$$Z_w = \frac{R_W \ \tanh(j\omega T_W)^\phi}{(j\omega T_W)^\phi} \tag{1}$$

where $T_W = \delta^2/D_a$ is a time constant, δ is the diffusion length, D_a is the diffusion coefficient, as well as R_w and ϕ being variable fitting parameters. Three equivalent circuits for modeling double layer, oxygen reduction in cathode, and methanol oxidation in anode are shown in Fig. 5(a)–(c).

3. Results and discussion

The results can be divided into three main sections: anode, cathode and membrane; but first of all the method of separation of these contributions out of the recorded impedance data will be presented.

Fig. 6 shows a typical spectrum recorded in anode polarization mode, i.e. with the cathode being supplied with hydrogen gas thus acting as a hydrogen reference electrode. If it is compared with a spectrum of the full cell, i.e. with the cathode being supplied with oxygen in the same frequency range (Fig. 7), it is possible to see that the smaller semi-circle occurring at higher frequencies (500 Hz to 60 kHz) is present in both spectra. In fact the magnitude and shape of this smaller, high frequency component does not vary between the two measurement modes at all and is always present regardless of any change in current density. Frequencies above 500 Hz are also a very strong indicator that chemical reactions are not included in this data since these take place at much larger time scales. It can thus be interpreted as behavior not specific to either electrode but
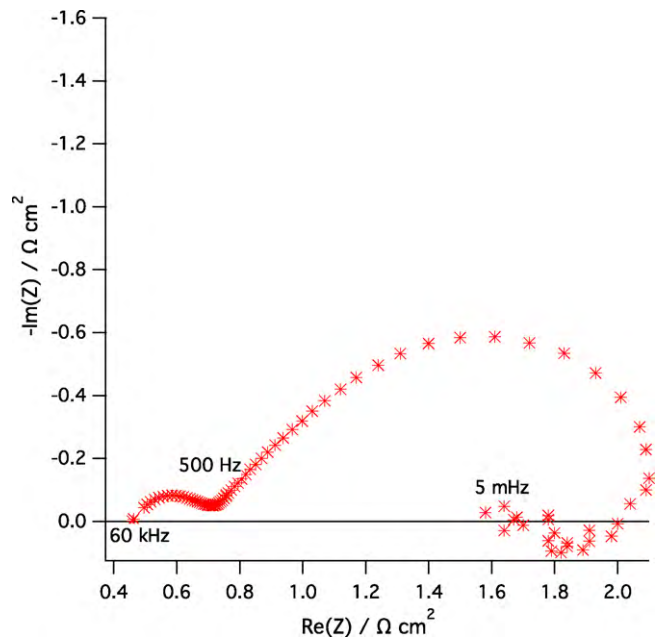

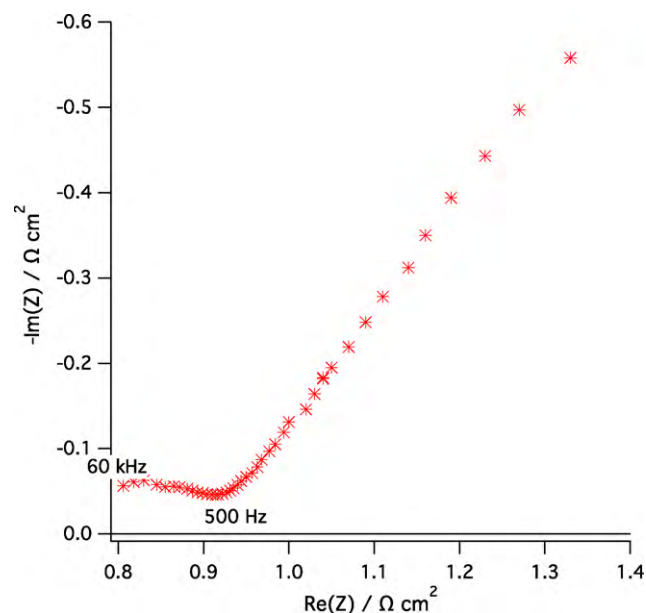**Fig. 6.** Full anode spectrum. Conditions: 0.035 ml min^{-1} methanol flow rate 60 °C, serpentine flow channel, 60 mA cm^{-2}.

Fig. 7. Enlargement of full cell spectrum. Conditions: 0.035 ml min^{-1} methanol flow rate, serpentine flow channel, 60 °C, 60 mA cm^{-2}.
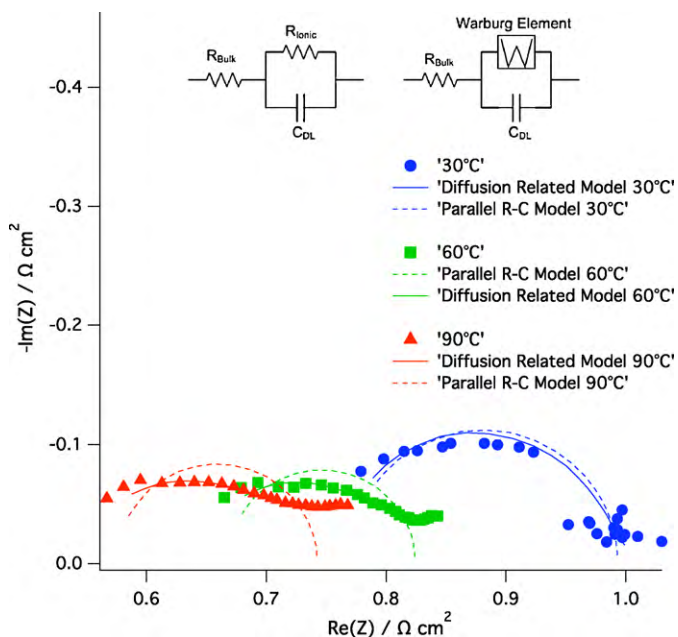
Fig. 8. Effect of temperature variation. Recorded data with model fits. Conditions: $0.14\,\mathrm{ml\,min^{-1}}$ methanol flow rate, parallel anode structure, 8 mA. Circuits: parallel R–C (left), diffusion related model (right). Frequencies: 500 Hz to 60 kHz.
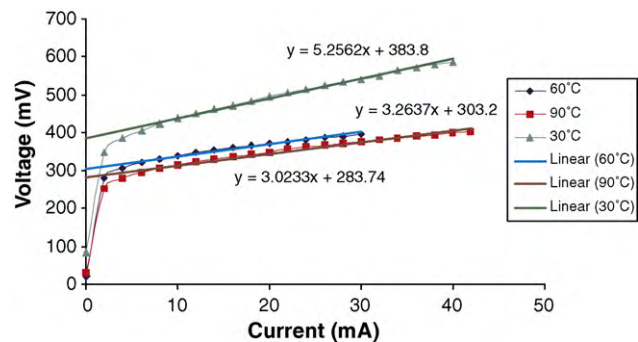

Fig. 9. Voltage versus current of the cell running in anode polarization mode. $0.14\,\mathrm{ml\,min^{-1}}$ methanol flow rate, serpentine flow channels, 8 mA.

arising from non-Faradaic processes such as double layer charging of both electrodes with the membrane.

Since it is possible to make a consistent and clear distinction between the two different semi-circular features at different frequencies, they will be treated separately for analysis in the following subsections.

3.1. Membrane and electrode interface

The first and main observation made from studying the phenomena occurring at higher frequencies is that there is a clear dependence of the position of the spectra along the horizontal axis (real part of impedance) on temperature. Fig. 8 shows this dependence with three different sets of experimental data each recorded at different temperatures: 30, 60 and 90 °C. It can be clearly seen that the higher the temperature the smaller the offset from the origin is. This also correlates nicely with the data recorded using polarization curves, although here it is not possible to separate the contributions to overall cell resistance. Fig. 9 shows how the slope of the linear portion, i.e. pure ohmic resistance decreases with increasing temperature. These resistance values should theoretically be due to pure ohmic components in the cell setup as they are free of any capacitor charging effects. They could be found in connecting wires, electrode connectors, electrode resistance and possibly the membrane itself. However, such strong temperature dependence can only be explained by membrane resistance, which has been proven to decrease with increasing temperature [31]. This argument leads to the conclusion that a substantial amount of the membrane resistance is free of any double layer charging effects and therefore its magnitude is shared between a pure ohmic resistance as well as an ohmic resistance coupled with a capacitance.

Fig. 8 not only shows experimental data but also fits using the models discussed earlier in Section 2.5 (also included on top of Fig. 8). These model fits are useful in being able to quantify various effects of operating parameters and allow a comparison with published values. Table 1 shows values of bulk resistance (R_{bulk}) and capacitor coupled resistance (R_{ionic}) using the parallel R–C model. Only values from this model are presented and analyzed here for two main reasons: the bulk resistance values do not deviate enough between the two models to warrant including the data, i.e. their absolute values and behavior are exactly the same as with the parallel R–C model; the parameter representing resistance in the Warburg element is not at all comparable with its supposed counterpart R_{ionic} in the parallel R–C model.

It is apparent that the magnitude of R_{bulk} is much higher than that of R_{ionic} but that both decrease by a similar amount: approximately 23% from 30 to 90 °C with the only exception being the bulk resistance of the serpentine flow field decreasing by 42% over this temperature range. Indeed, not only does the serpentine flow field show a larger decrease over the temperature range but it also consistently produces a higher bulk resistance than the parallel flow field does (20% increase averaged from three data sets). One anomaly in this set of data is present in that the value for R_{ionic} with a parallel flow field does not decrease from 60 to 90 °C, instead, it increases slightly. However, the increase is not substantial compared to the decrease that takes place from 30 to 60 °C and is therefore most likely a cause of a change in membrane hydration or such like which is very difficult to regulate. The published values for R_{bulk} are in the range $0.16\text{–}0.7\,\Omega\,\mathrm{cm^2}$ [20,34,35]. Our values are within the published range although they tend towards the upper limit and do exceed the upper limit at lower temperatures. However, this is understandable since this range of values found in literature correspond to operating temperatures of 60–90 °C.

Regarding the double layer capacitance which also shows a dependence on temperature, the limits of using two slightly different models become apparent. In three out of the four cases (varying flow field structure and equivalent fitting model) a substantial increase in the double layer capacitance is recorded. However in one case (parallel flow field using diffusion related model) the capacitance decreases slightly with increasing temperature even though it increases with the parallel R–C model (see Table 2).

Table 1
Bulk and capacitor coupled resistance values of different flow fields and temperatures.

Temp (°C)	R_{bulk} Parallel ($\Omega\,\mathrm{cm^2}$)	R_{bulk} Serpentine ($\Omega\,\mathrm{cm^2}$)	R_{ionic} Parallel ($\Omega\,\mathrm{cm^2}$)	R_{ionic} Serpentine ($\Omega\,\mathrm{cm^2}$)
30	0.77	1.01	0.22	0.26
60	0.67	0.83	0.16	0.22
90	0.58	0.58	0.17	0.20

Table 2
Double layer capacitance values of different models, flow fields and temperatures.

Temp (°C)	Parallel R–C ($F\,cm^{-2}$)	Increase (%)	Serpentine R–C ($F\,cm^{-2}$)	Increase (%)	Parallel Warburg ($F\,cm^{-2}$)	Increase (%)	Serpentine Warburg ($F\,cm^{-2}$)	Increase (%)
30	$3.88e^{-5}$		$4.09e^{-5}$		$3.39e^{-5}$		$2.35e^{-5}$	
60	$6.20e^{-5}$	60	$4.71e^{-5}$	15	$3.21e^{-5}$	−5	$2.98e^{-5}$	27
90	$6.69e^{-5}$	8	$1.35e^{-4}$	186	$2.93e^{-5}$	−9	$6.12e^{-5}$	105

Latham [16] reported a range of double layer capacitances from a literature survey. Although they are not obtained from DMFCs instead from hydrogen fuel cells, the same membrane type (Nafion) was used. Their values span four orders of magnitude ranging from $5e^{-5}$ to $2e^{-2}$ $F\,cm^{-2}$ with our values lying at the lower end of this spectrum.

The Warburg parameter which replaced the parallel resistor in the equivalent circuit model helped to improve the goodness of fit substantially. It reduced the Chi-Squared statistical test, which quantifies the goodness of fit, averaged over all data sets by one order of magnitude. Lasia [36] provided an in-depth description of diffusion models used in EIS. The generalized Warburg element used in our model is supposed to represent finite length diffusion in processes involving Faradaic reactions. Even though at the high frequency components we are currently discussing (>500 Hz) no Faradaic reactions take place, an analogy can still be made to the diffusion of charge carrying ions through the porous membrane electrode assemblies and membrane itself. Catalyst layers themselves are designed to be highly porous in order to increase the surface area of reactant sites, the so-called triple phase boundary between membrane, reactant mass and catalyst metal. Therefore it is highly plausible that a diffusion-like behavior is noted in the double layer charging characteristic of the cell.

3.2. Anode

Anode data was recorded in the so-called anode polarization mode as described in Section 2.4. Fig. 9 shows a polarization curve with the cell in this mode. It compares well with other such polarization curves that appear in literature [22,34], showing a high initial polarization resistance followed by a linear ohmic resistance. It does not, however, show mass transport limitations as a standard full cell polarization curve would do [22].

As was discussed at the beginning of Section 3 the spectrum obtained whilst running the cell in anode polarization mode corresponds to Fig. 6. We will now discuss the much larger semi-circle that occurs at lower frequencies (5 mHz to 500 Hz). This sort of frequency range makes it highly likely attributable to Faradaic processes. Indeed, another strong indicator for this presumption is that it is primarily a function of current density. It varies from being infinitely large at open circuit conditions and then shrinks in magnitude with increasing current density (although in fact it is not infinitely large and does close itself at frequencies much lower than 5 mHz but for the purpose of comparing it with conditions under load it may be taken as infinitely large). The two graphs in Fig. 10 attempt to show this dependence. Experimentally recorded data points are displayed and fitted with a line corresponding to the equivalent circuits of Fig. 5c.

Similar to the analysis in Section 3.1 two equivalent circuits have been fitted to the experimental data. Again, just by visual inspection it is possible to see that the equivalent circuit with the Warburg element is able to fit the data much better. The Chi-squared value is reduced from 0.174 to 0.077. The main difference in the shape of the fit between the two models is a straightening of the curve at higher frequencies, which is the principal reason the diffusion related circuit fits the experimental data better. This 45° line behavior has often been attributed to diffusion processes and the Warburg element [16].

3.2.1. Charge transfer resistance

As expected [18,20] the diameter of the semi-circle attributed to the charge transfer reaction of methanol at the anode decreases with increasing current density indicating an acceleration of the oxidation reaction. In the parallel R–C circuit the charge transfer resistance is quantified using a resistor in parallel with the rest of the circuit. In our extended circuit which includes the diffusion related Warburg element, the charge transfer resistance is con-
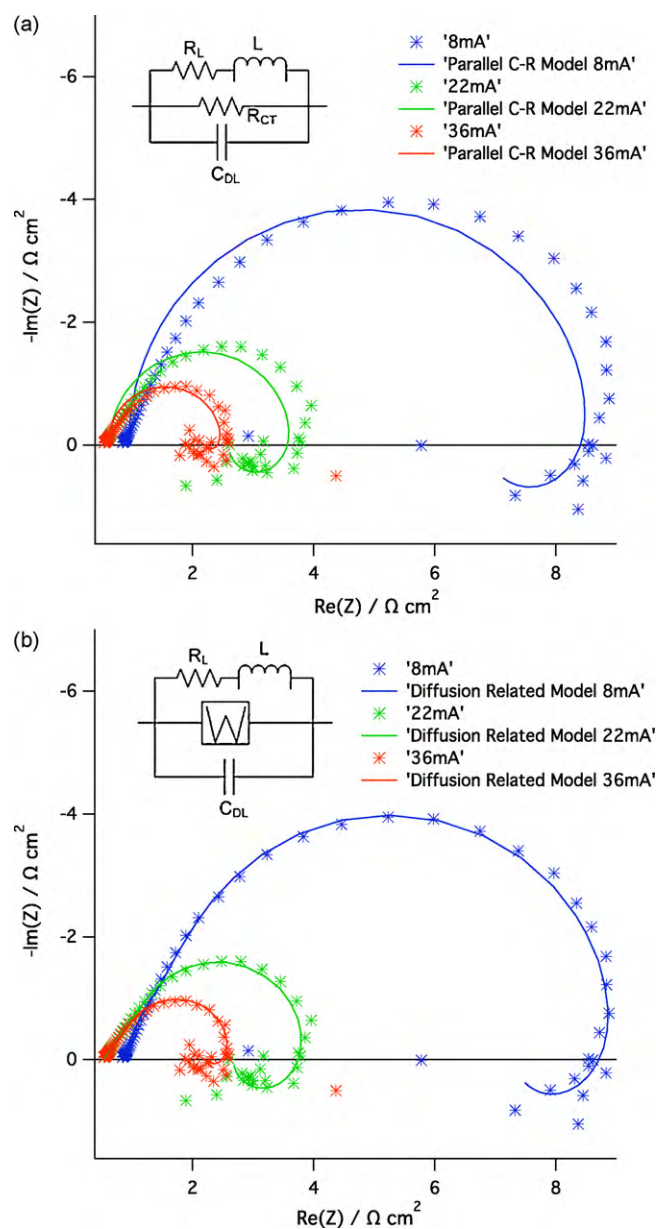

Fig. 10. Anode spectrum, varying current density. Experimental data fitted with (a) parallel R–C equivalent circuit, (b) diffusion related equivalent circuit. Conditions: Parallel flow channel, 0.14 ml min^{-1} methanol flow rate, 60 °C. Frequencies: 5 mHz to 500 Hz.
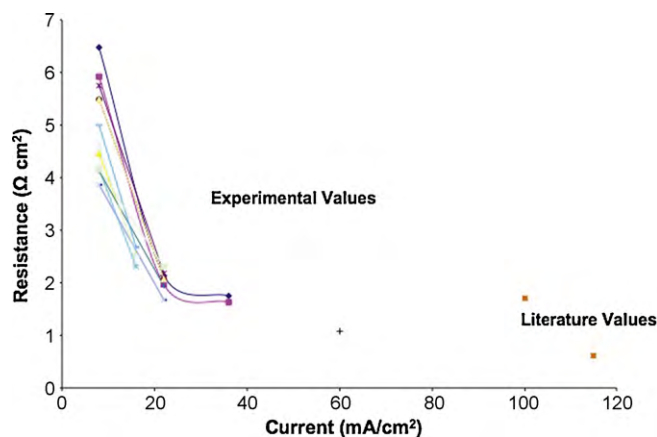
Fig. 11. Experimental values of charge transfer resistance as a function of current density including literature values [18,20].

Fig. 12. Experimental values of inductance as a function of current density including literature values [18,20].

tained in the Warburg R_W parameter and can be directly compared to R_{CT} in the nature of its behavior.

Fig. 11 shows the strong dependence of charge transfer resistance on current density. The x-axis has been extended to allow a comparison with literature values which were all taken at much higher current densities: $1.705\,\Omega\,cm^2$ at $100\,mA\,cm^{-2}$ [18], $0.612\,\Omega\,cm^2$ at $115\,mA\,cm^{-2}$ [20] and a range of $1.8–5.5\,\Omega\,cm^2$ for various current densities [34]. Data points connected by a line are from tests performed under the same parameters (except for current density). Up to a current density value of $20\,mA\,cm^{-2}$ the slope of the linear decrease in charge transfer resistance is reasonably similar and steep in all cases. This is plausible since we know that under open circuit conditions (i.e. zero current density) the charge transfer resistance goes towards infinity. After $20\,mA\,cm^{-2}$ the slope decreases dramatically and if extrapolated would approach zero resistance at infinite currents. This is supported by the fact that the literature values found would approximately lie on such a curve. In our work, the point at $60\,mA\,cm^{-2}$ is the highest current density value at which an impedance spectrum was measured. Therefore, if one assumes that the charge transfer resistance would continue to behave according to this hyperbolic correlation, then there must be some other mechanism limiting the ability to draw more current from our test cell.

3.2.2. Inductance

As seen in Fig. 10(a), an inductive loop occurs at the lowest frequencies of the spectrum and correlates nicely with expectations from literature research (Section 2.5). The value of inductance varies strongly with several operating parameters. An increase in current density causes a decrease in the magnitude of inductance. Fig. 12 shows this dependency. The logarithmic scale on the inductance axis shows the exponential decrease of inductance with increasing current. This behavior can be explained by a decreased coverage of CO due to higher kinetic rates of charge transfer reducing the phase lag of current behind voltage. These findings correlate nicely with the investigations reported in [37], where EIS was used to show that at high cell potentials the oxidation of intermediate CO was the rate limiting mechanism in the anode reaction. At lower cell potentials the reaction of intermediate CO is no longer the rate limiting mechanism and thus no inductance is observed. At medium potentials a transition phase between CO oxidation and initial CO formation being the rate limiting mechanism is also observed.

There is also a direct dependency of inductance on temperature (see Fig. 13). The inductance decreases exponentially with increasing temperature. This can be explained by a much faster oxidation
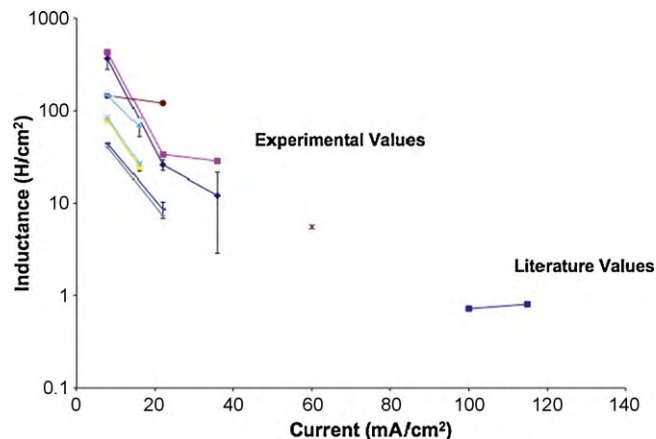
of intermediate carbon monoxide at higher temperatures and thus leading to less coverage of reactive sites.

A correlation with the type of flow field can also be seen. The parallel channels consistently exhibit a larger inductance effect than the serpentine flow field. The exact reasons behind this are likely to be fairly complex. From previous works using laser induced fluorescence to study the two phase flow in the anode microchannels [30,38], it can be seen that reactant flow through the parallel channels was highly non-uniform. This could possibly be a factor in slower intermediate carbon monoxide oxidation. Furthermore it can be seen that removal of carbon dioxide bubbles from the parallel microstructure was impeded when compared to the serpentine structure. One must also bear in mind that when the parallel flow channels were in use on the anode there was still a serpentine flow field on the cathode. This asymmetry could lead to the reactant flow being impeded further due to the catalyst layer being pressed onto the flow field structure in places other than just the channel ribs. Thus a number of factors from using different flow field patterns could have an influence on the inductance magnitude presented here. Nevertheless, from experience gathered during these experiments as well as previous tests conducted with this single cell setup, it is known that the serpentine flow field produces far more stable operation than the parallel flow field (hence the use of only serpentine structures on the cathode in this work). Thus a lower inductance value could be one precursor for more stability in cell operation.

As seen in Fig. 13 the inductance values span one order of magnitude. Indeed these values are orders of magnitude off literature values, which range from 0.3 to $0.8\,H\,cm^{-2}$ [18,20,34,35],
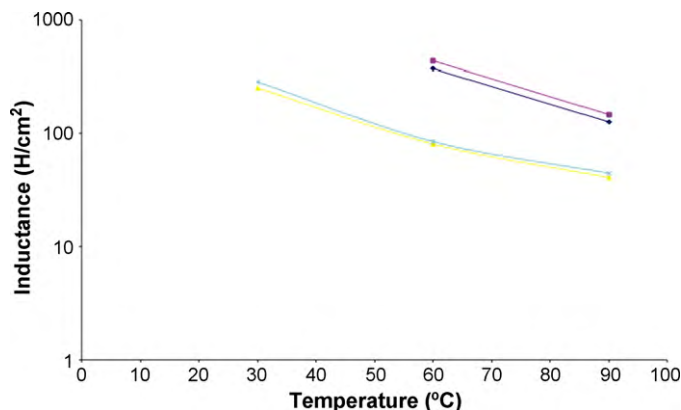

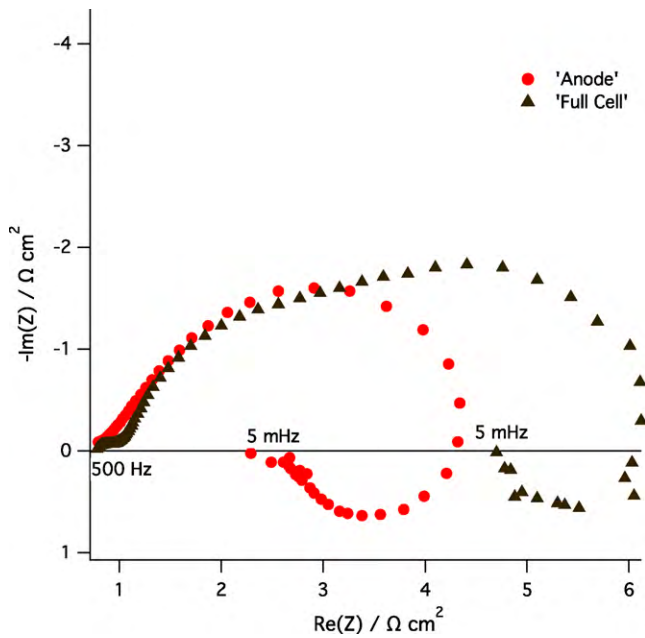**Fig. 13.** Experimental values of inductance as a function of temperature.

Fig. 14. Comparison of anode spectrum to full cell spectrum. Conditions: serpentine anode, 0.14 ml min^{-1} methanol flow rate, 90 °C, 22 mA.

making their validity highly questionable. However, since none of the literature values come from micro-fuel cells, one must always be careful in comparing values directly to literature. Microsized fluid channels and the fact that no diffusion layer is employed on the anode side could even be the reason for such a dramatic increase in inductance. The fact that the spectra recorded in this micro-fuel cell show more diffusion-like behavior in that the spectra exhibit more flattening behavior when compared to those of macro-DMFCs in literature, means that there are higher concentration gradients within the electrode structure. This would also help explain the extremely high values for inductance since intermediate CO would take much longer to become oxidized.

3.2.3. Faradaic pseudo-capacitance

There is some disagreement in literature regarding the dependence of capacitance on current density. Piela et al. [20] showed a good correlation between increasing capacitance and increasing current density. They explained this behavior by the fact that, at
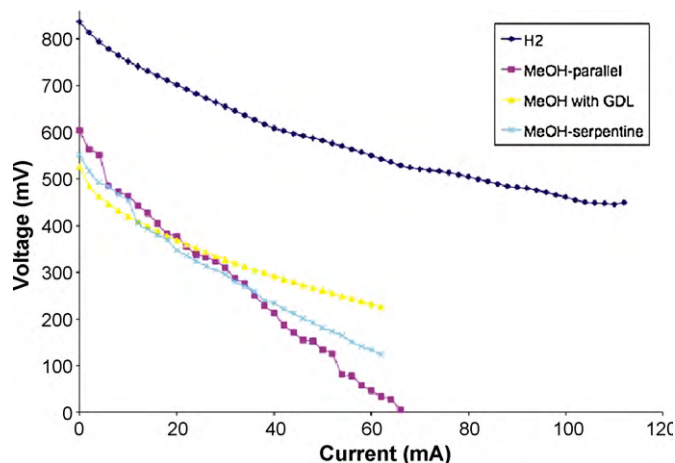
higher current densities, there is decreased coverage by absorbed CO (see Section 3.2.2), thus increasing the available catalyst area for charge carrying ions. However, Hsu et al. [34] reported a decrease in capacitance with increasing current density. Care must be taken to look at the details of their modeling. Piela et al. [20] used a model such as the one shown in Fig. 5(c) with simple resistor instead of Warburg element, whereas Hsu et al. [34] used the same model but with the capacitor replaced with a constant phase element. The use of a distributed element, which is similar in behavior and physical meaning to the Warburg element used in this study, allows for a much better fit of the experimental data. Piela et al. [20] reported themselves, that their component values were associated with a large positive error of up to 100%. In nine out of eleven cases of modeling our experimental data, a decrease in capacitance comes as a result of an increase in current density. This behavior obviously contradicts the explanation given by Piela et al. [20]. However, the absolute values of capacitance, which in our case are extremely low, do fit into their theory since our inductance values are extremely high, therefore indicat-
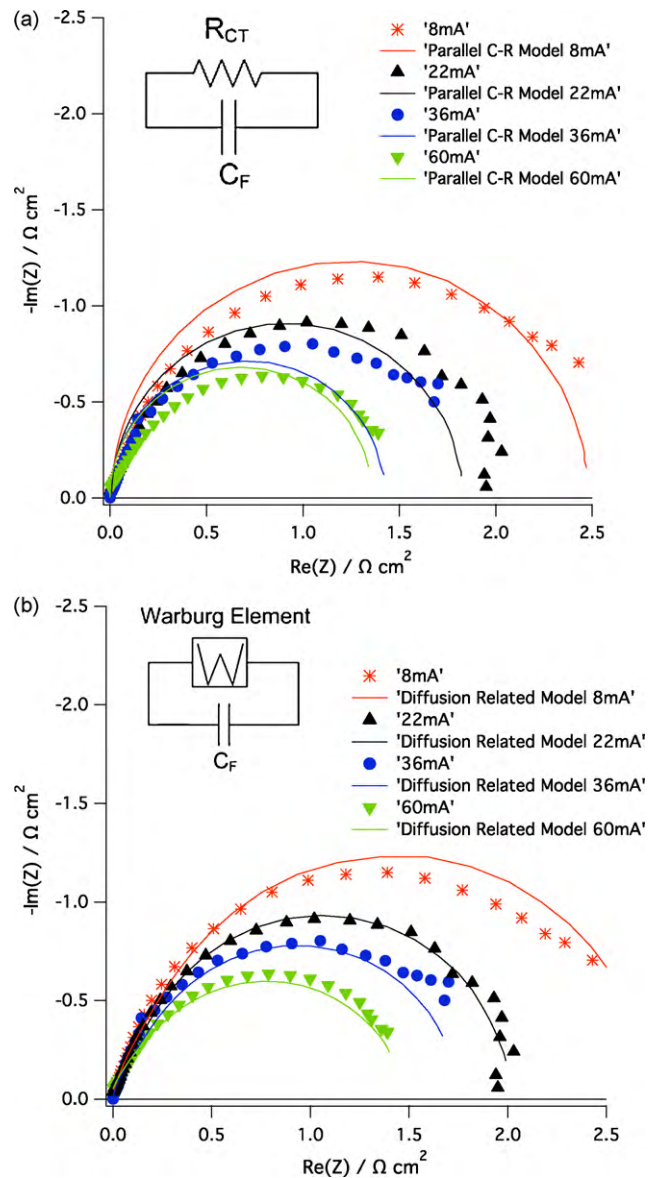

Fig. 16. Cathode impedance spectra. 0.5 Hz to 3 kHz. Conditions: 0.14 ml min^{-1} methanol flow rate, 60 °C, parallel anode flow channels. Data fit for (a) the parallel R–C circuit and (b) the diffusion related circuit.

Fig. 15. Comparison of a H$_2$/O$_2$ cell with a MeOH/O$_2$ cell. Conditions for MeOH data: 0.14 ml min^{-1} methanol flow rate, 90 °C.

ing high intermediate carbon monoxide coverage decreasing the capacitance.

3.2.4. Contribution of anode impedance to full cell

Fig. 14 shows a comparison between an impedance spectrum recorded in anode polarization mode (anode) and one recorded in the full cell mode. It can clearly be seen that the anode impedance loop constitutes the majority of that of the full cell. A polarization curve of the two modes was also recorded (shown in Fig. 15). There three methanol measurements were conducted: one with a serpentine anode, one with a parallel anode and one with a serpentine anode and a gas diffusion layer on the cathode side. It is obvious that the performance is considerably worse using methanol than hydrogen. The open circuit voltage is 200–300 mV lower and the slope of the curves is far steeper indicating a much higher resistance.

3.3. Cathode

As was explained in Section 2.4, subtraction of the recorded anode impedance spectrum from the recorded full cell impedance spectrum yields the cathode impedance spectrum. The non-Faradaic contribution discussed in Section 3.1 is eliminated, since it appears in both the anode and full cell spectra. Fig. 16(a) shows the calculated cathode spectra (individual data points) and their dependence on current density. The curves represent an equivalent circuit fit using a resistor parallel with a capacitor. The same experimental data are also plotted again in Fig. 16(b) with a fit using the diffusion related circuit from Fig. 5(b). Similar to the anode spectra the magnitude of the arc decreases with increasing current density, again showing the acceleration of the Faradaic reaction at higher current densities.

The frequency range and shape of the plots in Fig. 16(b) is in good accordance with the results presented in [17]. Although spectra were recorded from much lower frequencies (5 mHz), the data between 5 mHz and 0.5 Hz in both the anode and full cell recorded spectra is very prone to noise and thus, when they are subtracted from each other, yield yet more random data. This does not necessarily imply that important information has been omitted and goes
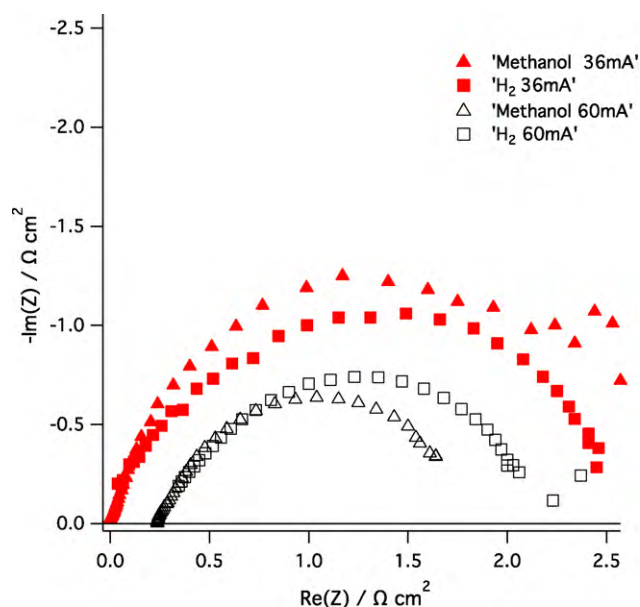
back to the discussion about the presence of an inductive loop in cathode data. Piela et al. [20] attribute the cathode inductive loop to absorbed intermediate carbon monoxide resulting from the oxidation of methanol that has diffused through the membrane. This is very plausible, however, if one considers the fact that cathode data are calculated from two recorded spectra, in which methanol is present in both and in which there is no reason to assume a difference in the amount of methanol crossover, then the effect of methanol crossover in the impedance spectra should cancel out, once these are subtracted from each other.

3.3.1. Verification of cathode data

By running the cell in the classical direct hydrogen configuration, i.e. supplying hydrogen to the anode and oxygen to the cathode and measuring the impedance whilst applying the same assumption that hydrogen oxidation impedance is negligible compared to oxygen reduction impedance, we obtain the impedance

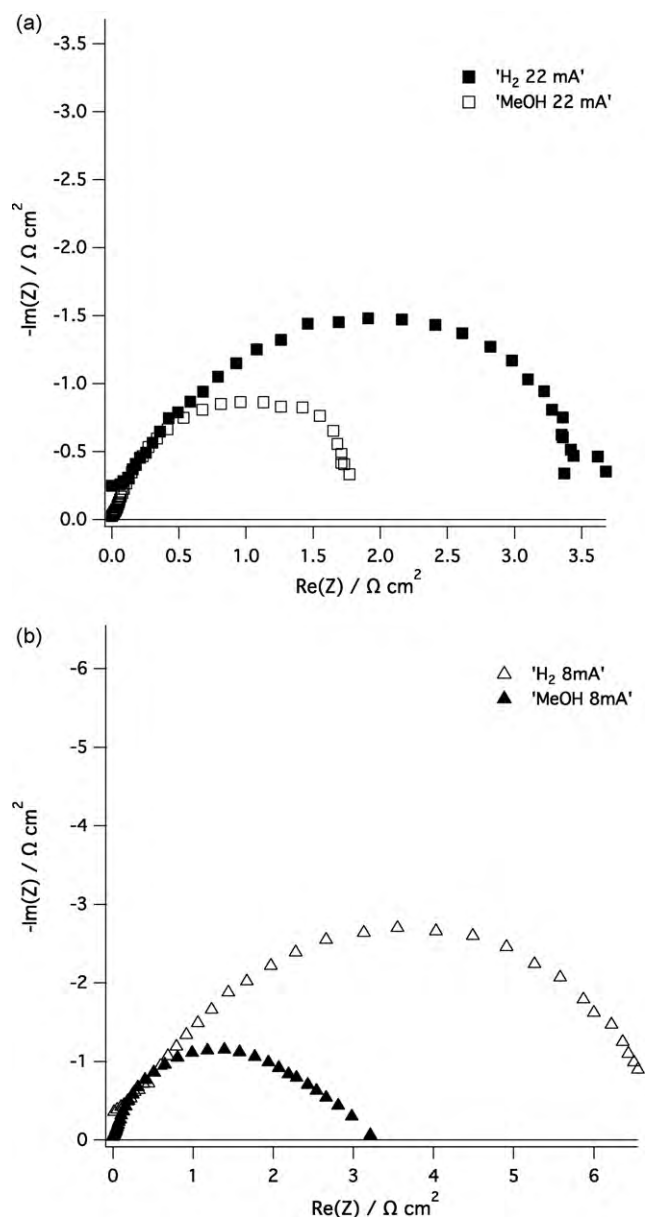Fig. 18. Comparison of H_2/O_2 data with cathode spectra from DMFC at (a) 22 mA and (b) 8 mA. MeOH data conditions: parallel, 0.14 ml min^{-1} methanol flow rate, 60 °C. Frequencies 0.5 Hz to 3 kHz.

Fig. 17. Comparison of H_2/O_2 data with cathode spectra from DMFC at 60 and 36 mA. MeOH data conditions: parallel, 0.14 ml min^{-1} methanol flow rate, 60 °C. Frequencies 0.5 Hz to 3 kHz.

of the oxygen reduction reaction at the cathode. The experimental data obtained using this method are obviously free of any methanol crossover effects and can be used to verify the theory that methanol crossover impedance should cancel out when subtracting anode from the full cell spectra. Fig. 17 shows a comparison of directly recorded impedance spectra from a H_2/O_2 cell (H_2 in legend) and the cathode impedance spectra from the DMFC (MeOH in legend).

In Fig. 17 data sets recorded at 60 and 36 mA are shown. It is possible to see that the shape and magnitude of the two different data sets at the same current density are not far off each other. However, when the current density is increased further (Fig. 18) then the correlation between the different data sets worsens substantially. This is a strong indicator for the fact that methanol crossover does influence the calculated cathode spectra and is not eliminated by using this method. It is well known that methanol crossover plays a much larger role at lower current densities [39] and this can be seen in the figures above. As current density decreases, the calculated cathode spectra (MeOH) become smaller compared to their counterparts from the H_2/O_2 test. Since they represent the difference between anode and full cell spectra, this means that the anode spectrum has become larger relative to the full cell spectrum under conditions of higher methanol crossover. This is plausible, since, when recording the impedance of the full cell, methanol crossover is not likely to influence the impedance as much as it is when supplying the cathode with hydrogen and thus introducing a negligible reaction in terms of impedance.

3.3.2. Comparison with literature values

Piela et al. [20] report a capacitance value of $0.06\,F\,cm^{-2}$ at $69\,mA\,cm^{-2}$ for their cathode data. This is approximately three to four times greater than the values obtained from fits on data collected in this study, which range from 0.015 to $0.025\,F\,cm^{-2}$ at current densities of 36–60 mA. As explained in Section 3.2.3, there is some disagreement in the literature as to the effect of current density on the capacitance value. Nevertheless, the impact has never been anywhere near as strong as the exponential dependency of R_{CT}.

Unfortunately, an extensive analysis of equivalent circuit component values could not be achieved since noise-free data were much harder to obtain. Also, the effects of varying the operating parameters such as methanol flow rate, temperature as well as the anode structure could not be deduced from the obtained cathode data.

4. Conclusion

EIS was used as a diagnostic tool for a micro-DMFC. Even though there has so far been limited use of impedance spectroscopy on DMFCs and does not appear to have been used on micro-DMFCs, reproducible results conforming with known theory on electrochemical phenomena in DMFC and in accordance with analysis from other EIS studies on DMFC could be obtained in this study. The impedance results gathered could show a clear distinction between the different electrochemical phenomena occurring in DMFCs. Especially the distinction between double layer charging and Faradaic reactions was invariably more pronounced than in other work found in literature. However, when comparing the performance of this test cell with those from literature it appears to be considerably worse. Unlike the standard DC diagnostic tools, impedance spectroscopy was able to separate the various cell contributions and identify the methanol oxidation reaction in general as the main limiting factor. More specifically, coverage of intermediate carbon monoxide on catalyst reactive sites hindering further oxidation is the most pronounced single mechanism contributing to cell performance loss. Comparison with spectra from an H_2/O_2 cell allowed partial validation of the impedance theory developed by Müller and Urban [17]. It can be seen that the recorded spectra using this technique are heavily influenced by methanol crossover, especially at low current densities, making noise-free cathode data much harder to achieve. The analysis using impedance spectroscopy in this work was also able to show a definite impact of the anode flow channel structure on the magnitude of inductance at the anode. Definite reasons for this still have to be clarified, but a strong connection can be made to the better removal of carbon dioxide gas bubbles in the serpentine structure. The effect of increased temperature manifests itself both as better conductivity of the membrane and better oxidation of intermediate carbon monoxide at the anode, thus improving cell performance vastly. In this parametric study the effect of varying methanol feed rate in a range of very high stoichiometries was also investigated. However, no direct dependence on this parameter in the ranges tested could be identified.

References

[1] M. Baldauf, W. Preidel, Journal of Power Sources 84 (1999) 161–166.
[2] R. Rashidi, I. Dincer, G.F. Naterer, P. Berg, Journal of Power Sources 187 (2009) 509–516.
[3] S.K. Kamarudin, W.R.W. Daud, S.L. Ho, U.A. Hasran, Journal of Power Sources 163 (2007) 743–754.
[4] G.Q. Lu, C.Y. Wang, Journal of Power Sources 144 (2005) 141–145.
[5] N.T. Nguyen, S.H. Chan, Journal of Micromechanics and Microengineering 16 (2006) R1–R12.
[6] T.S. Zhao, R. Chen, W.W. Yang, C. Xu, Journal of Power Sources 191 (2009) 185–202.
[7] J. Zhang, PEM Fuel Cell Electrocatalysts and Catalyst Layers, Springer-Verlag, London, 2008.
[8] W.R. Baumgartner, P. Parz, S.D. Fraser, E. Wallnofer, V. Hacker, Journal of Power Sources 182 (2008) 413–421.
[9] J. Deseure, Journal of Power Sources 178 (2008) 323–333.
[10] J.P. Diard, B. Le Gorrec, C. Montella, C. Poinsignon, G. Vitter, Journal of Power Sources 74 (1998) 244–245.
[11] H. Kuhn, B. Andreaus, A. Wokaun, G.G. Scherer, Electrochimica Acta 51 (2006) 1622–1628.
[12] J. Li, C.W. Moore, D. Bhusari, S. Prakash, P.A. Kohl, Journal of the Electrochemical Society 153 (2006) A343–A347.
[13] W. Mèrida, D.A. Harrington, J.M. Le Canut, G. McLeand, Journal of Power Sources 75 (1998) 139–143.
[14] T.E. Springer, T.A. Zawodzinski, M.S. Wilson, S. Gottesfeld, Characterization of Polymer Electrolyte Fuel Cells Using AC Impedance Spectroscopy, Los Alamos National Laboratory, Electronic and Electrochemical Materials and Devices, Los Alamos, 1996.
[15] S. Wasterlain, D. Candusso, D. Hissel, F. Harel, P. Bergman, P. Menard, M. Anwar, Journal of Power Sources 195 (2010) 984–993.
[16] R. Latham, Masters thesis, University of Victoria, 2004.
[17] J.T. Müller, P.M. Urban, Journal of Power Sources 75 (1998) 139–143.
[18] J.T. Müller, P.M. Urban, W.F. Hölderich, Journal of Power Sources 84 (1999) 157–160.
[19] J.P. Diard, N. Glandut, P. Landaud, B. Le Gorrec, C. Montella, Electrochimica Acta 48 (2003) 555–562.
[20] P. Piela, R. Fields, Z.P. elenay, Journal of the Electrochemical Society 153 (2006) A1902–A1913.
[21] U. Krewer, H.K. Yoon, H.T. Kim, Journal of Power Sources 175 (2008) 760–772.
[22] J.C. Amphlett, B.A. Pebbley, E. Halliop, A. Sadiq, Journal of Power Sources 96 (2001) 204–213.
[23] H. Fukunaga, T. Ishida, N. Teranishi, C. Arai, K. Yamada, Electrochimica Acta 49 (2004) 2123–2129.
[24] H. Fukunaga, K. Okajima, M. Sudoh, Journal of Power Sources 139 (2005) 9–14.
[25] G. Li, P. Pickup, Electrochimica Acta 49 (2004) 4119–4126.
[26] F. Lufrano, V. Baglio, P. Staiti, A. Stassi, A.S. Aricè, V. Antonucci, Journal of Power Sources (2010), doi:10.1016/j.jpowsour.2009.11.130, in press.
[27] X. Zhao, X. Fan, S. Wang, S. Yang, B. Yi, Q. Xin, G. Sun, International Journal of Hydrogen Energy 30 (2005) 1003–1010.
[28] S.H. Yang, C.Y. Chen, W.J. Wang, Journal of Power Sources 195 (2010) 3536–3545.
[29] T. Yuan, Z. Zou, M. Chen, Z. Li, B. Xia, H. Yang, Journal of Power Sources 192 (2009) 423–428.
[30] C. Weinmüller, G. Tautschnig, N. Hotz, D. Poulikakos, Journal of Power Sources 195 (2010) 3849–3857.
[31] F. Büchi, G. Scherer, Journal of Electroanalytical Chemistry 404 (1996) 37–43.
[32] B. Conway, W. Pell, Journal of Solid State Electrochemistry 7 (2003) 637–644.

[33] J.R. Macdonald, Impedance Spectroscopy: Theory, Experiment and Applications, John Wiley and Sons, New Jersey, 1987.
[34] N.Y. Hsu, S.C. Yen, K.T. Jeng, C.C. Chien, Journal of Power Sources 161 (2006) 232–239.
[35] Y. Wang, G. Au, E.J. Plichta, J.P. Zheng, Journal of Power Sources 175 (2008) 851–860.
[36] A. Lasia, in: B.E. Conway, J. Bockris, R.E. White (Eds.), Electrochemical Impedance Spectroscopy and Its Applications, Modern Aspects of Electro-chemistry, vol. 32, Kluwer Academic/Plenum Publishers, New York, 1999, pp. 143–248.
[37] G. Wu, L. Li, B.Q. Xu, Electrochimica Acta 50 (2004) 1–10.
[38] C. Weinmüller, N. Hotz, A. Mueller, D. Poulikakos, International Journal of Multiphase Flow 35 (2009) 722–760.
[39] R O'Hayre, S.W. Cha, W. Colella, F.B. Prinz, Fuel Cell Fundamentals, Wiley & Sons, New York, 2006.